

Investigation on compressive behavior of Cu–35Ni–15Al alloy at high temperatures

CONG LI, JIAN CHEN*, WEI LI, YONGLE HU, YANJIE REN, WEI QIU, JIANJUN HE, JIANLIN CHEN

School of Energy and Power Engineering, Changsha University of Science and Technology, Changsha, Hunan, 410004, China

Microstructures and mechanical properties of Cu–35Ni–15Al alloy in cast and porous states were studied by scanning electron microscopy and compression tests. The influence of porosity, deformation temperature and loading rate on mechanical properties of the two kinds of alloys was investigated. The results show that the as cast alloy and porous alloys have almost the same phase constitution: Cu rich phase, Ni rich phase and K intermetallics. The yield strength of porous alloys increases continuously with decreasing porosity, the relationship between porosity and yield stress follows Gibson-Ashby equation. With decreasing deformation temperature, the yield strength of as cast alloy and porous alloy increase. With the increase of loading rate, the yield strength of these alloys shows an increasing trend. After compression, the microstructure of as cast alloy is more uniform, and porous alloys are more prone to have localized deformations.

Keywords: *Cu–35Ni–15Al alloy; compression; deformation temperature; loading rate*

© Wrocław University of Technology.

1. Introduction

Molten carbonate fuel cell (MCFC) is the most promising energy conversion device which transforms the chemical energy into electric power. High efficiency of power generation, zero pollution, and possibility of exhaust heat recovery are the main advantages that make MCFC attractive for a variety of applications [1]. Anode is a vital component of the MCFC. Due to the existence of pores and good permeability, the porous metals are widely used in the electrodes of fuel cells. The pores provide channels for the movement of fuel gas and free electrons [2]. The anode of MCFC now is mostly made from porous Ni based alloys. Yet the scarcity of Ni resources has hindered the wider use of MCFC. Cheaper anode material, copper, which can replace nickel, has been explored and found to be a more suitable material. Copper alloys, with their combination of high thermal conductivity and acceptable mechanical strength and toughness over a wide range of temperatures, are likely the best candidate for complex structural applications subjected to conditions of extreme heat flux

under load [3]. Yuasa et al. reported that an addition of nickel in copper anode could improve the electrochemical property. It also has been found that the high temperature performance of anodes can be improved dramatically by adding Al [4]. Because of good conductivity and sintering properties, porous Cu–Ni–Al alloy is considered to be an ideal material for the anode of MCFC.

Since the electrodes need to be cooled with gas, thermal shocks may occur at the anode/electrolyte interface. In addition, the porous alloys employed for structural components in MCFC applications are often subjected to high temperature and compression loads simultaneously. The interaction of high temperature and compression load leads to intense stress concentration in the components of porous alloy. Such a concentration of stress around a pore often results in catastrophic failure of components. Due to these concerns, investigations aimed at increasing the heat-resistance of metallic alloys are needed. However, the current research on MCFC anode materials is mainly aimed at the porous Ni alloy [5–12], few papers focus on the mechanical properties of porous Cu alloys at high temperatures. Thus, it is noted that, despite the fact that porous Cu alloys are attractive mate-

*E-mail: chenjian_513@126.com

rials for MCFCs, only limited data are available in the literature. P. Lei *et al.* studied the method of preparation of Cu–Ni pre-alloyed powders [13], J. Chen *et al.* also investigated the porous Cu–35Ni–15Cr alloy by numerical simulation, to clarify the influence of pore size, pore shape, loading stress and deformation temperature on this alloy properties [14]. But the factors that affect the high temperature properties of porous Cu–Ni–Al alloy have not been reported yet. In order to provide a theoretical basis for the application of porous Cu–Ni–Al copper alloy as an anode material in MCFC, a novel porous alloy (Cu-35 wt.% Ni-10 wt.% Al) has been prepared on the basis of concepts and results of earlier works [13–17]. Attention was focused mainly on elucidating the effect of porosity, deformation temperatures and loading rates on the compressive mechanical properties in this alloy compared with the as cast alloy with identical composition.

2. Experimental details

2.1. Preparation of as cast alloy

The quality of raw materials used in the experiment can affect the function of the product greatly. In this experiment, electrolytic copper produced by Daye Nonferrous Metals Company, grade Cu-CATH-2, with purity 99.99 %, electrolytic nickel produced by Jinchuan Group, grade Ni9996, with purity 99.98 % and electrolytic aluminum with purity 99.86 %, were used. The raw materials-copper, nickel and aluminum, in accordance with the proportion: 35 wt.% Ni, 10 wt.% Al, were put into a graphite crucible and subjected to thermal treatment in an intermediate frequency furnace, at 1500 °C for 1h. 3 ‰ refining agent and slag were added into the molten metal. After mixing, refining and slagging, the liquid metal was finally casted into ingots. From the as-cast thick slab, cylindrical samples of 8 mm diameter and 12 mm length were formed using electrical discharge machining. A thin layer was removed from the outer surface by polishing prior to further experimentation. The results of chemical analysis of the alloy are shown in Table 1.

Table 1. Composition of as cast Cu alloy (mass. %).

Elements	Al	Ni	Cu
Composition	9.65	34.3	56.05

2.2. Preparation of porous alloys

Porous Cu-35 wt.% Ni-10 wt.% Al alloys were fabricated using the pre-alloyed powders. The pre-alloyed powders were prepared by atomization technology which was mentioned in reference [13]. The morphology of powders was nearly spherical. Pre-alloyed powders were then packed into a graphite mould. The green samples were subsequently heat treated under controlled temperatures to remove stearic acid and finally sintered in a tube furnace in hydrogen environment to avoid oxidation. The final sintering processing was carried out at 1050 °C for 2 h. The forming of Cu–Ni–Al sintering products was done by hot pressing sintering under 5600 Pa pressure. The results of chemical analysis of the alloy are shown in Table 2.

Table 2. Composition of porous Cu alloy (mass.%).

Elements	Al	Ni	Cu
composition	10.2	36.47	53.33

2.3. Methodology

The microstructure of the alloys was determined using a field emission scanning electron microscope (FE-SEM), equipped with an energy dispersive X-ray spectrometer (EDX) to measure the elements concentration. The concentration data were obtained using a 20 kV and 15 mA beam. The mechanical properties of the samples (Φ 8 mm \times 12 mm, cylindrical shape) of various porosities were assessed by compression testing at high temperatures in a RDL05 electronic creep-fatigue testing machine. Deformation temperatures were set at 600 °C, 650 °C and 700 °C. In order to ensure uniform heating of the samples, after achieving the assumed temperature, the samples were heated for 30 min, then the data started to be collected. For each condition 3 samples were deformed. Before the experiments,

samples were carefully polished. The porosity values were measured using the Archimedes principle (ASTM, C373-72).

3. Results and discussion

3.1. As-cast alloy

Fig. 1 shows a SEM image of an as cast Cu–35Ni–10Al alloy sample before compression test; Table 3 lists the elements concentrations at the points a, b, c, d, marked in Fig. 1. Because the Cu–Ni–Al alloy was prepared by casting, a small amount of other impurities was inevitably introduced. From the analysis of SEM images and EDS results, it can be found that the dark gray area in Fig. 1, such as point a, is the Ni rich phase. The Cu rich region, such as point b, is bright in the picture. In addition, some granular, acicular, blossom plum shaped Ni rich phases exist in the Cu matrix, and in the Ni rich phase region there also are granular, needle like, rod like Cu rich phases. Such particles belong to K intermetallic phase.

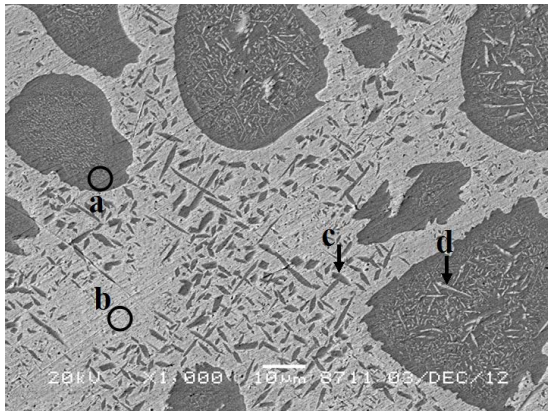


Fig. 1. SEM image of as-cast Cu–35Ni–10Al alloy before compression test.

Table 3. EDS results of as-cast Cu–35Ni–10Al alloy.

Elements(wt.%)	Cu	Ni	Al	Fe impurities
a	27.17	51.06	16.88	4.90
b	60.89	27.83	7.54	3.74
c	33.58	45.61	15.64	5.17
d	61.39	28.10	7.40	3.12

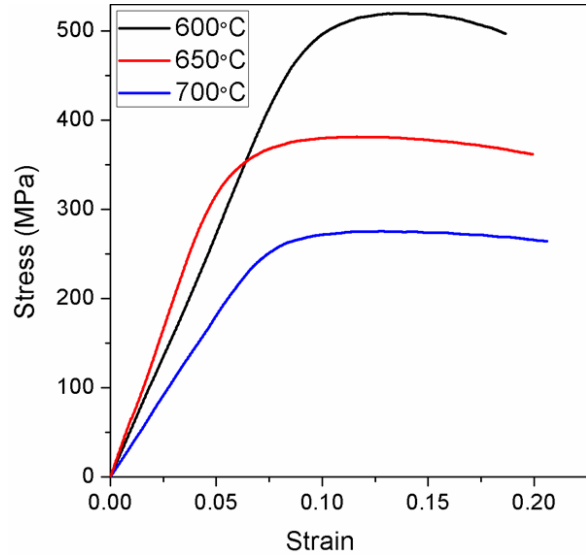


Fig. 2. Typical stress-strain curve of as-cast alloy at different temperatures.

In order to evaluate the mechanical properties of the as cast alloy, high temperature compression experiments with a loading rate of 10^{-3}s^{-1} were carried out. The tests were performed at 600 °C, 650 °C, 700 °C; a typical stress-strain curve is shown in Fig. 2. The yield strengths of the as cast alloys at different temperatures are shown in Table 4. It can be seen that with the increasing of temperatures, the strength value decreases from 520 MPa to 270 MPa. This is mainly caused by the following reasons: (1) with temperature increasing, the kinetic energy of metal atoms and the number of slip systems increase, which improves the dislocation mobility in a certain extent; (2) in high temperature environment, it is easy for alloys to have dynamic recovery and recrystallization, thus the strain hardening process is eliminated and the materials are softened; (3) elevated temperatures significantly reduce the intergranular shear resistance, so that the grain boundary slip becomes easier, thereby alleviating the stress concentration between the grains. The deformation behavior of as cast Cu–35Ni–10Al alloy at high temperature is governed by the above factors.

In order to assess the effect of strain rate on mechanical properties of Cu–35Ni–10Al alloy at high temperature, compression test was carried out un-

der different loading rates ($10^{-2}/s$, $10^{-3}/s$, $10^{-4}/s$) at $650\text{ }^{\circ}\text{C}$. Typical stress-strain curve is shown in Fig. 3. As can be seen from the graph, the curve can be divided into three stages: elastic deformation stage (the start of linear increase), the stage of plastic deformation and local plastic deformation stage. At the stress drop stage, external force exceeds the maximum value and contraction of a portion of material cross-section occurs. The external force decreases and the deformation continues to increase. The yield strength values of this alloy are listed in Table 4. It can be seen from the Table, that along with an increase of loading rate, the strength values increase from 260 MPa to 490 MPa. When the strain rate is high, the external macroscopic deformation is fast, but the internal microstructure deformation is delayed, defects such as dislocations cannot move rapidly, which produces the accumulation and aggregation and improves the deformation resistance. On the other hand, during the short deformation process, the internal state of this alloy cannot fully complete the dynamic recovery and recrystallization, which also results in an improvement of the yield stress.

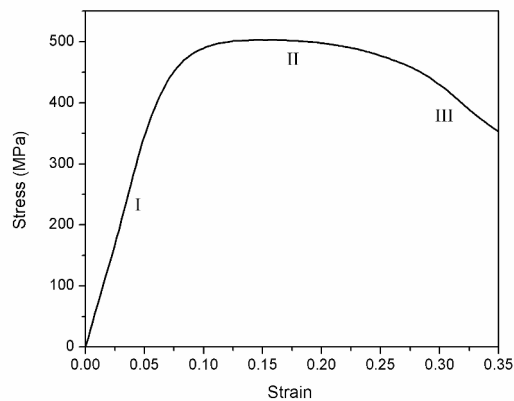


Fig. 3. Typical stress-strain curve of as-cast alloy with a loading rate of 10^{-2} s^{-1} .

Visual observation of a broken cylinder of the compressive specimens revealed that the overall fracture path was oriented at roughly 45 degrees to the compressive loading axis, as shown in Fig. 4a. Therefore, it is plausible to conclude that the frac-

Table 4. The yield stress of as cast alloys.

Deformation temperature	600 °C	650 °C	700 °C
Yield stress	520 MPa	360 MPa	270 MPa
Loading rate	10^{-4} s^{-1}	10^{-3} s^{-1}	10^{-2} s^{-1}
Yield stress	260 MPa	360 MPa	490 MPa

ture of the compressive specimens is caused by the shear stress. The fracture failure process can be described by the following steps. In the early stage of the fracture, the plastic deformation of ductile phase begins to form dislocations. With the increase of stress, during the sliding process, the dislocations meet the brittle phase and are hindered by them, which leads to a dislocation concentrated zone and results in a local shear band and cracks initiated on defects in the sample. Fig. 4b shows the SEM microstructure of Cu-35Ni-10Al alloy after compression test. For the samples failed upon moderate strain rate loading (10^{-3} s^{-1}) it can be found that after deformation, the grains are elongated in the direction perpendicular to the compression force. The whole deformed microstructure is more or less uniform. When the grain boundary is damaged, with the further grain sliding, damage gradually extends to the formed holes and the deformation capacity of the alloy is obviously weakened. Since there is no enough deformation to coordinate the adjacent grains, the grain boundary cracking, such as the black areas in Fig. 4b, occurs.

3.2. Porous alloys

The SEM microstructure of porous Cu-35Ni-10Al alloy with a porosity of 32.3 % is shown in Fig. 5. As can be seen in Fig. 5, the bonds between pre-alloyed powders are obvious, and it makes the alloy have better moldability and higher strength. The black areas in the images are the pores, although their shape is not regular. The alloys consist of two phases; gray areas represent the Ni rich phase, and bright areas are Cu rich phase. Fig. 5b shows the microstructure at higher magnification. Compared with as cast Cu-35Ni-10Al alloy, it can be seen that the phase constitution of the porous alloy has not changed too much.

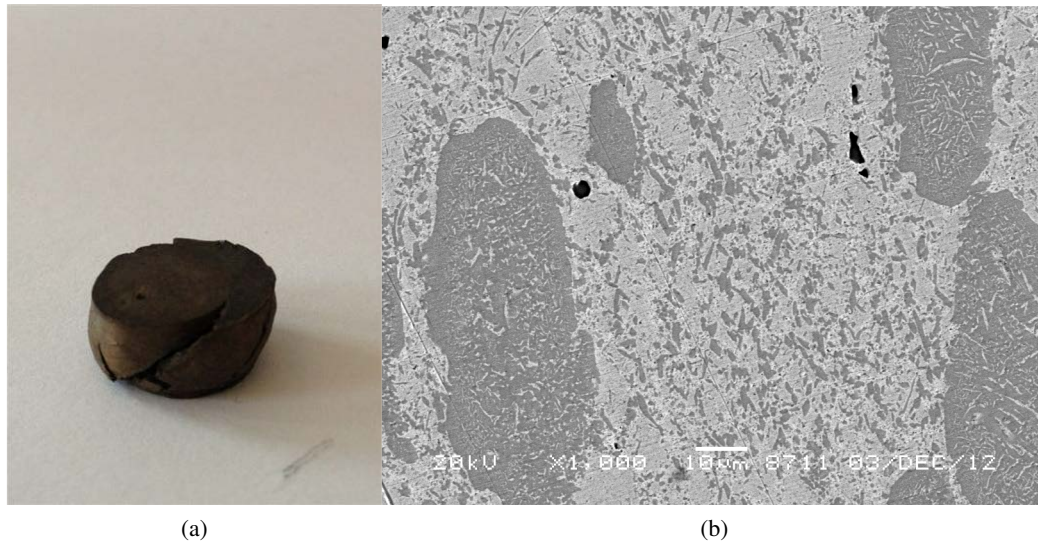


Fig. 4. Broken cylinder of the compressive specimens (a), SEM microstructure of as cast alloy after deformation (b).

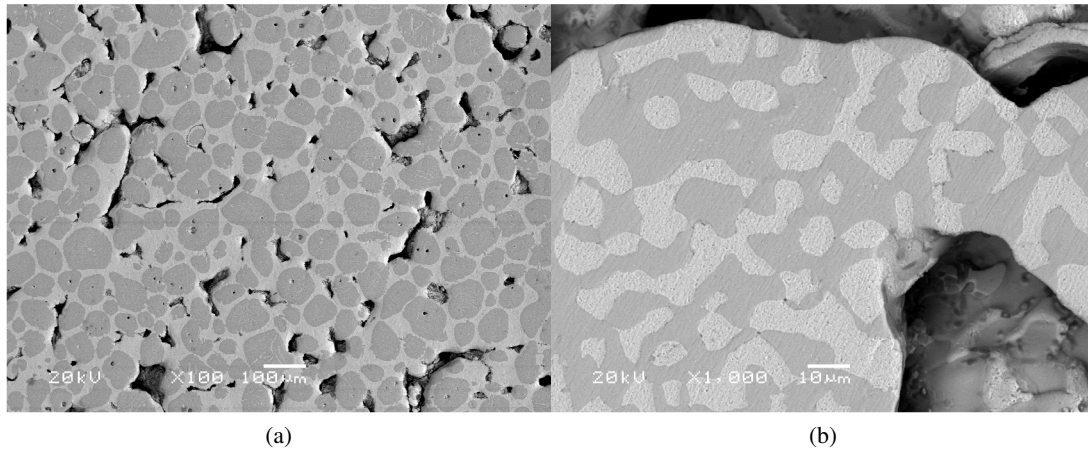


Fig. 5. SEM microstructure of porous alloy before deformation: (a) low magnification, (b) high magnification.

The influence of porosity, deformation temperature, loading rate on the compressive properties of porous Cu–35Ni–10Al alloy is shown in Fig. 6–9. From the current images, it can be found that the porous alloys obviously have different deformation behaviors as compared to as cast alloy. The yield strength of porous alloys in a range of 80 MPa to 230 MPa is much lower than that of as cast alloy. Stress-strain curves of porous alloys can be divided into three stages: elastic region, stress plateau region and densification region. In the first stage,

it can be seen that the effect of alloy porosity, deformation temperature and loading rate on the elastic modulus is very weak, but the yield strength of the alloys exhibits a higher sensitivity. Fig. 6 shows the stress-strain curves of porous alloys with different porosities. It can be concluded that with the increasing porosity, the yield stress decreases. When porosity increases from 24.5 % to 32.3 %, the drop of yield stress is not significant, but when the porosity increases to 41.5 %, the yield stress decreases sharply. In addition, when the porosity is

41.5 %, the strain interval of stress plateau region is narrower than in the other two samples.

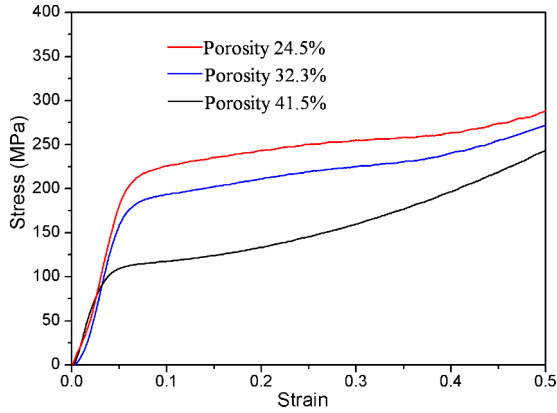


Fig. 6. Stress-strain curves of porous alloys with different porosities.

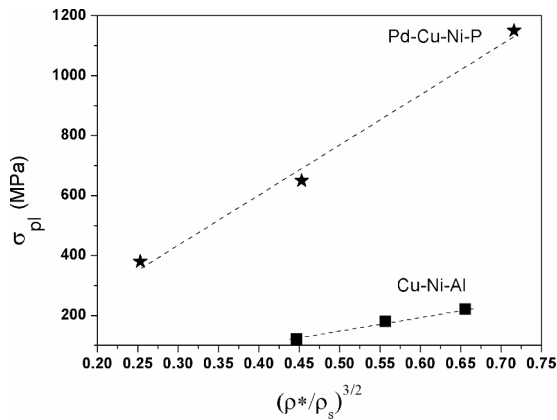


Fig. 7. The yield strength as a function of relative density of porous metal.

The effect of porosity on yield stress is nonlinear. Using the Gibson-Ashby equation, the relationship between porosity and yield stress can be quantitatively studied [18]:

$$\frac{\sigma_{pl}}{\sigma_{ys}} = C \left(\frac{\rho^*}{\rho_s} \right)^{\frac{3}{2}} \quad (1)$$

$$\sigma_{pl} = \sigma_{ys} C \times \left(\frac{\rho^*}{\rho_s} \right)^{\frac{3}{2}} \quad (2)$$

σ_{pl} is the plateau stress (the yield strength of porous materials), σ_{ys} is the yield strength of solid

materials, ρ^* is the density of porous metal, ρ_s is the density of solid material, C is an experimental constant, and $\frac{\rho^*}{\rho_s}$ is the relative density of porous metal. By transformation of equation 1, we can get equation 2. Applying the experimental data (as listed in Table 5) in the equation 2, it was found that they fit the theoretical formula very well (as depicted in Fig. 7). The tangent deduced from equation 2 and denoted by the dash line in Fig. 7, which represents $C\sigma_{ys}$, is a constant. Comparing the data with the parameters obtained for Pb-Cu-Ni-P porous alloy, it was found that the two alloys show similar linear trend in $\sigma_{pl} - \left(\frac{\rho^*}{\rho_s}\right)^{3/2}$ map, although the tangent is different. That difference may be attributed to the different intrinsic properties of the alloys and experimental conditions. But both alloys obey the Gibson-Ashby law very well.

Table 5. Parameters of porous alloys.

Cu-Ni-Al	Porosity %		
	24.5	32.3	41.5
Plateau stress (MPa)	220	180	120
Pb-Cu-Ni-P [19]	Porosity %		
	20	41	60
Plateau stress (MPa)	1150	650	380

Fig. 8 shows the effect of deformation temperature on porous alloys. Two series of compression tests with loading rates of 10^{-3}s^{-1} and 10^{-4}s^{-1} were performed. As can be seen from the graphs, the deformation temperature has a profound influence on the yield stress. The yield strength as a function of temperature is depicted in Fig. 8c. With the increase of deformation temperature, the yield strength of the three alloys decreases, but compared to as cast alloy, the temperature sensitivity of porous alloy is lower. The pores have reduced the sensitivity. In addition, two trend lines with loading rates of 10^{-3}s^{-1} and 10^{-4}s^{-1} are almost parallel to each other, that means the deformation loading rate has not a significant influence on the temperature sensitivity of the porous alloys.

Fig. 9 shows the effect of loading rate on porous alloy. The changes of the mechanical properties of the alloys with different loading rates were studied at 650 °C and 700 °C. As can be seen from the

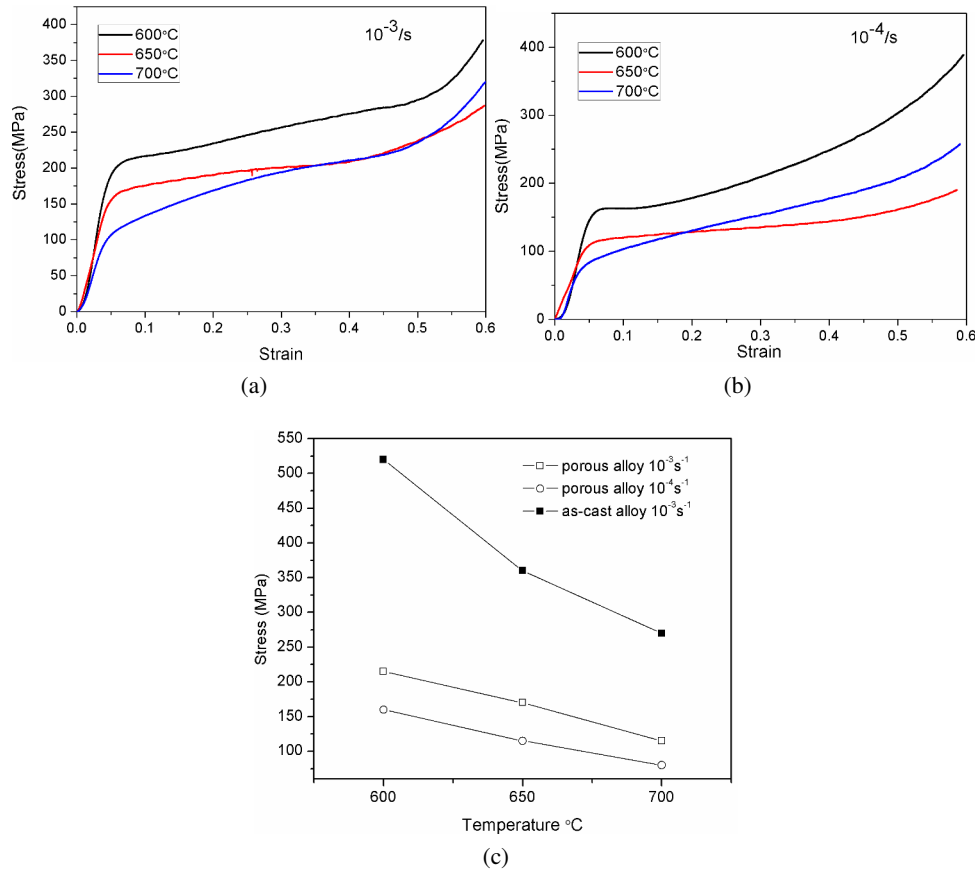


Fig. 8. Mechanical properties of porous alloys under different temperatures: (a) stress-strain curves at the load rate of $10^{-3}s^{-1}$, (b) stress-strain curves at the load rate of $10^{-4}s^{-1}$, (c) the relationship between yield stress and deformation temperature.

graphs, the loading rate has a great impact on yield strength. The relationship between yield strength and loading rate for three alloys is described in Fig. 9c. With the increase of loading rate, the yield strength of the three alloys shows an increasing trend, but compared to the as cast alloy, the loading rate sensitivity of porous alloys is lower. The pores have reduced this kind of sensitivity for the alloys. In addition, two trend lines at the temperature of 650 °C and 700 °C are almost parallel to each other; it implies that the temperature has not an important influence on the loading rate sensitivity of porous alloys.

Fig. 10 shows a SEM image of microstructure of a porous alloy after the compressive test. Because of the presence of large pores in the alloy and the irregularity of these pores, compared with the as cast alloy, the internal deformation process

of porous samples is not uniform. The grain size fluctuation lead to a heterogeneous deformation behavior, thus the local internal instability is easy to happen. When the strain exceeds the stress plateau region and enters the densification region, the inner edges of the pores are compressed and contact each other, which results in the slits, as shown in Fig. 10.

4. Conclusions

Compared with Ni based alloys, porous copper alloys have been found to be a more suitable material for the use in MCFC because of their combination of high thermal conductivity and acceptable mechanical strength. In order to provide a theoretical basis and an experimental support for the application of porous copper alloy in MCFC field, this study concerned an analysis of the effect of

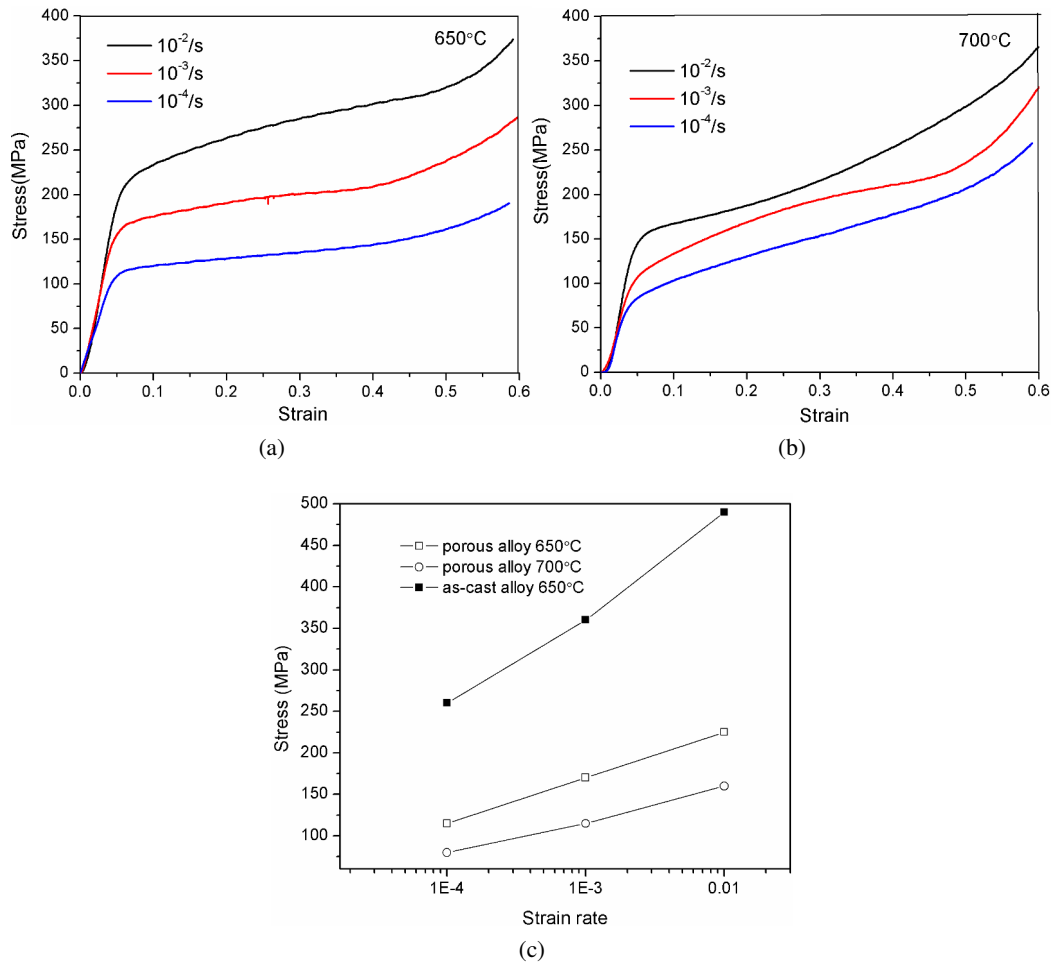


Fig. 9. Mechanical properties of porous alloys under different loading rates: (a) stress-strain curves at the temperature of 650 °C, (b) stress-strain curves at the temperature of 700 °C, (c) the relationship between yield stress and loading rate.

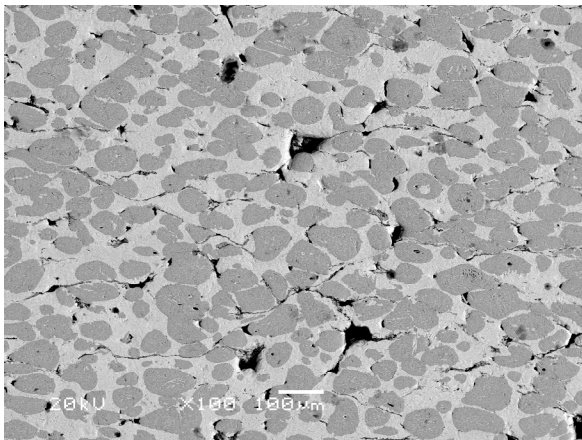


Fig. 10. SEM microstructure of porous alloy after deformation (porosity: 32.3 %, temperature: 650 °C, loading rate: $10^{-3} s^{-1}$).

deformation temperature and loading rate on the compressive properties of as cast alloy and porous alloys (Cu–35Ni–10Al). The key conclusions can be summed up as follows:

- (1) The as cast alloy and porous alloys have almost the same phase constitution: Cu rich phase, Ni rich phase and K intermetallics.
- (2) The strength of as cast alloy is significantly higher than that of porous alloys. The yield strength values of as cast alloy and porous alloy increase continuously with decreasing deformation temperature. With the increase of loading rate, the yield strength of these alloys shows an increasing trend. But the as cast alloy possesses higher sensitivity. The

yield strength of porous alloy increases with the decrease in porosity, which follows the Gibson-Ashby relationship.

- (3) The deformed microstructure of as cast alloy after compression is homogeneous, and the porous alloys are more prone to local deformation.

Acknowledgements

This work is supported by the Open Research Fund of Innovation Platform of Efficient & Clean Utilization of Energy (12K079) and Open Research Fund of Key Laboratory of Hunan Province (2014NGQ004). The authors are grateful to the National Natural Science Foundation of China (51075044).

References

- [1] FRANGINI S., *J. Power Sources*, 182 (2008), 462.
- [2] ANDUJAR J.M., SEGRUA F., *Renew. Sust. Energ. Rev.*, 13 (2009), 2309.
- [3] LI G., THOMAS B.G., STUBBINS J.F., *Metall. Mater. Trans. A*, 31 (2000), 2491.
- [4] TSUYOSHI N., VINAY G., YOSHIMI O., MEITEN K., RAM N.S., ALAIN T., ETIENNE D., *J. Power Sources*, 104 (2002), 181.
- [5] CHAWLA N., DENG X., *Mat. Sci. Eng. A-Struct.*, 390 (2005), 98.
- [6] CEDERGREN J., MELIN S., LIDSTROM P., *Powder Technol.*, 160 (2005), 161.
- [7] WEE J.H., *Mater. Chem. Phys.*, 98 (2006), 273.
- [8] KIM D., LEE I., LIM H., LEE D., *J. Power Sources*, 109 (2002), 347.
- [9] KIM Y.S., LEE K.Y., CHUN H.S., *J. Power Sources*, 99 (2001), 26.
- [10] WEE J.H., *Mater. Chem. Phys.*, 101 (2007), 322.
- [11] LEE H., LEE I., LEE D., LIM H., *J. Power Sources*, 162 (2006), 1088.
- [12] KIM G., MOON Y., LEE D., *J. Power Sources*, 104 (2002), 181.
- [13] LEI P., CHEN J., LI W., REN Y.J., QIU W., CHEN J.L., *Appl. Mech. Mater.*, 303 (2013), 2490.
- [14] CHEN J., HUANG Z.H., LI W., REN Y.J., HE Z., QIU W., HE J.J., CHEN J.L., *Key Eng. Mater.*, 573 (2014), 105.
- [15] WANG B., ZHANG E., *Int. J. Mech. Sci.*, 50 (2008), 550.
- [16] KIM Y.S., CHUN H.S., *J. Power Source*, 84 (1999), 80.
- [17] HWANG E.R., PARK J.W., KIM Y.D., KIM S.J., KANG S.G., *J. Power Source*, 69 (1997), 55.
- [18] QIAO J.C., XI Z.P., TANG H.P., WANG J.Y., ZHU J.L., *Mater. Trans.*, 49 (2008), 2919.
- [19] TAKESHI W., MAKOTO K., *J. Mater. Res.*, 21 (2006), 1041.

Received 2013-12-31
Accepted 2014-04-28